



Cite this: *Nanoscale Adv.*, 2022, **4**, 761

## Bioinspired nanoscale hierarchical pillars for extreme superhydrophobicity and wide angular transmittance†

Cheonji Lee,‡<sup>ab</sup> Seungmuk Ji,‡<sup>c</sup> Sunjong Oh,<sup>a</sup> Seungchul Park,<sup>a</sup> Youngdo Jung,<sup>a</sup> Jinkee Lee<sup>\*b</sup> and Hyuneui Lim  <sup>\*ad</sup>

Hierarchical structures in nature provide unique functions for living organisms that can inspire technology. Nanoscale hierarchical structured surfaces are essential to realize the dual functions of non-wetting and transparency for applications such as cover glasses and windows; however, these structures are challenging to fabricate. In this study, nano-hierarchical structured glass surfaces were fabricated using multi-step colloidal lithography and etching to obtain tunable morphology. Nanostructured surfaces of mono-pillar structures of diameter 120 and 350 nm and hierarchical-pillar structures of their combinations exhibited superhydrophobicity after perfluoropolyether coating. In particular, the hierarchical nanosurfaces showed excellent non-wetting properties with the apparent, advancing, and receding water contact angles exceeding 177° and contact angle hysteresis below 1°. Water bouncing behaviors – contact time, spreading diameter, and shape of the bouncing motion were also evaluated according to the Weber number to examine the robustness of superhydrophobicity. Hierarchical nanosurfaces showed larger spreading diameters than mono-nanosurfaces with 14 bounces, indicating minimal energy loss from friction, as can be explained by the effective slip length. Furthermore, the nano-hierarchical structures exhibited better transmittance for wide angles of incidence up to 70° than mono-nanostructures owing to their reduced scattering area and multi-periodicity.

Received 12th November 2021

Accepted 23rd December 2021

DOI: 10.1039/d1na00806d

rsc.li/nanoscale-advances



<sup>a</sup>Department of Nature-Inspired Nanoconvergence Systems, Korea Institute of Machinery and Materials, 156 Gajeongbuk-Ro, Yuseong-Gu, Daejeon, 34103, Republic of Korea. E-mail: helim@kimm.re.kr; Fax: +82-42-868-7933; Tel: +82-42-868-7106

<sup>b</sup>School of Mechanical Engineering, Sungkyunkwan University, 2066, Seobu-Ro, Jangan-Gu, Suwon, Gyeonggi-Do, 16419, Republic of Korea. E-mail: lee.jinkee@skku.edu; Fax: +82-31-295-1937; Tel: +82-31-299-4845

<sup>c</sup>Yonsei Institute of Convergence Technology, Yonsei University, 85 Songdogwahak-ro, Yeonsu-gu, Incheon 21983, South Korea

<sup>d</sup>Department of Nano-mechatronics, University of Science and Technology, 217 Gajeongbuk-Ro, Yuseong-Gu, Daejeon, 34113, Republic of Korea

† Electronic supplementary information (ESI) available: Table S1; minimum and maximum capillary pressure ( $P_c$ ) and the effective slip length ( $b_{eff}$ ) of samples. The  $P_c$  of long pillars are marked with L and that of short pillars are marked with S; Movie S1; contact angle measurement. Attaching a water droplet on samples;  $S_{120}$ ,  $S_{350}$ ,  $S_{NH1}$ , and  $S_{NH2}$ . Volume of droplet is 10.3  $\mu$ l; Movie S2; droplet impact motion. Droplets impact on  $S_{NH2}$  with different dropped height; 80, 230, and 450 mm (Weber number; 48, 140, and 290). The volume of droplet is 8.6  $\mu$ l. The process is recorded at 3000 frames per second (fps) and shown at 30 fps; Movie S3; number of bouncing. Droplets bounce on samples;  $S_{120}$ ,  $S_{350}$ ,  $S_{NH1}$ , and  $S_{NH2}$ . The dropped height is 10 mm and volume of droplet is 8.6  $\mu$ l. The process is recorded at 3000 frames per second (fps) and shown at 30 fps. See DOI: 10.1039/d1na00806d

‡ Both authors contributed equally as first authors.

## 1. Introduction

Hierarchical structures are effective in realizing smart biological behavior in nature by implementing or reinforcing various surface functionalities, such as self-cleaning, antireflection, antibiofouling, water harvesting, structural color, and drag reduction.<sup>1,2</sup> These amazing properties enabled by hierarchical structures can be observed in the lotus leaf,<sup>3–6</sup> pitcher plant,<sup>7–11</sup> moth eye,<sup>12–16</sup> butterfly wings,<sup>17</sup> cicada wings,<sup>18</sup> Namib desert beetle's back,<sup>19–21</sup> and shark skin.<sup>22–25</sup> In particular, the introduction of a hierarchical nanostructure on transparent surfaces can lead to significant performance enhancement for the developing applications such as the cover glass of photovoltaics, building and car windows and lenses of optical sensors.<sup>26–28</sup> However, the implementation of nanoscale hierarchical structures on transparent surfaces is challenging because of the current lack of controllable and cost-effective nanofabrication techniques and lack of knowledge of the role of nano-hierarchies in wetting and optical properties.

The superhydrophobic surface of lotus leaves has a micro/nano hierarchical structured wax layer that exhibits a high contact angle and a low sliding angle. The microbump- and nanopillar-based hierarchical structures enhance the wetting properties compared to the hydrophobic chemical surface by reducing the contact area and the loss of the kinetic energy of

the water droplets at the interface between water and the structures.<sup>19,20</sup> The antireflective surface of the moth eye has ordered nanopillar structures, creating an interface at which the refractive index changes gradually. Consequently, the nanopillar structures largely suppress Fresnel reflection for a broad range of wavelengths as well as wide angles of incidence compared to optical coatings based on the quarter-wavelength principle.<sup>29-31</sup> Several studies have attempted to induce the combination of superhydrophobic and antireflective functional surfaces by fabricating the nanostructures on a transparent substrate. Park *et al.* demonstrated a nanotextured fused silica wafer using a multiple coating layer and subsequent etching steps. The subwavelength-tapered conical structures with high aspect ratios and large packing densities resulted in superhydrophobicity and omnidirectional transparency.<sup>32</sup> Furthermore, Lin *et al.* reported transparent superhydrophobic glass surfaces with nanopatterns fabricated using a femtosecond laser with exceptional water repellency and thermostability.<sup>33</sup> However, these surfaces were not successful in exhibiting improved non-wetting with dynamic droplets and transparency for wide angles because they utilized simple mono-structures unlike the hierarchical structures in nature. Therefore, hierarchical nanoscale surface development is required to understand extreme non-wetting properties and superior angular antireflective effects for the practical application of nanoscale dual roughness.

To date, the fabrication of hierarchical structures has been limited for the micro–nano hierarchy and has been performed *via* expensive, complex, and time-consuming methods such as electron beam lithography, nanoimprint lithography, photolithography, and hybrid approaches with laser or plasma treatment;<sup>34</sup> while the hierarchical structure at the nanoscale has not been well reported owing to the delicate complicated multistep process and restriction on the preparation of nanomasks. Colloidal lithography, also called nanosphere lithography, offers great advantages due to its high throughput and low cost.<sup>35</sup> Recently, Xu *et al.* reported the fabrication of periodic three-dimensional hierarchical silicon nanotubes using the selected and repeated etching of polystyrene nanospheres and deposited nickel.<sup>36</sup> Fang *et al.* produced silicon metastructures using a multi-step etching of a polystyrene nanosphere layer.<sup>37</sup> Although hierarchically aligned nanostructures have been demonstrated, the reported fabrication process is very delicate, and shows critical dependence on the etching conditions because only one size of polystyrene nanospheres was used as a mask.

In this study, we used a simple nanofabrication process to demonstrate a nanoscale hierarchical pillar-structured surface with tunable morphology and a two-tier solid fraction of low values. The manufactured hierarchical nanosurface was investigated to understand its wetting behavior and transmittance. Effectively, superhydrophobicity *via* water bouncing behavior after a low surface tension chemical coating as well as broad-band antireflection up to an incident angle of 70° were observed, demonstrating the excellent properties of the hierarchical nanosurface. The proposed nanofabrication method and the resulting hierarchical nanostructures imply that the bio-inspired nanopillar surfaces provide high-performance

functionality and can be expanded for various practical applications such as solar cells, windows, lenses, exterior materials of home appliances, and bio-devices.

## 2. Experimental section

### 2.1 Fabrication process of nanostructure

4 kinds of samples were prepared as the mono-structured nanopillars,  $S_{120}$  and  $S_{350}$ , and hierarchical nanopillars,  $S_{NH1}$  and  $S_{NH2}$ .  $S_{120}$  and  $S_{350}$  indicate the nanopillars made by using 120 nm PS NPs and 350 nm PS NPs, respectively.  $S_{NH1}$  and  $S_{NH2}$  indicate the hierarchical nanopillars made by using combinations of 120 nm PS NPs and 350 nm PS NPs with different size reduction times.

To prepare an etching mask, 10 wt% commercial colloidal polystyrene nanoparticles solution (Polyscience, Inc.) was used by diluting with ethanol (Aldrich) in an appropriate ratio according to the size of the nanoparticle, to control the solvent evaporation. The size distributions of the NPs were  $120 \pm 7$  and  $350 \pm 14$  nm, respectively. The nanoparticle assembly was generated by dropping the prepared nanoparticle solution using a micropipette with a few microliters on top of a hydrophilic supporting plate partially immersed in a deionized water bath. At the three-phase contact point, the nanoparticle assembly was floated on the water surface as an evaporating solvent, and then a certain area of the assembly was picked up using a 1 × 1 inch quartz glass substrate. Then, the size of the assembled nanoparticles on quartz glass was reduced to 20% using O<sub>2</sub> plasma inside the reactive ion etching chamber (All for System Inc.) to aid the etching by attaining the distance between the NPs. Anisotropic etching was followed in a mixture of CF<sub>4</sub>, H<sub>2</sub>, and O<sub>2</sub> gases. After etching, the remaining nanoparticles on the structures were removed using O<sub>2</sub> plasma. To fabricate nanoscale hierarchical structured surfaces; first, quartz was etched with 120 nm PS NPs using the same method to fabricate nanopillars. Subsequently, 350 nm-sized PS NPs were placed on the nanostructure, and the same process was repeated for size reduction of nanoparticles, glass etching, and removal of the remaining nanoparticles. The difference between the structures of  $S_{NH1}$  and  $S_{NH2}$  was determined by controlling the size reduction time of 350 nm PS NPs in the 2nd step. The size reduction time for  $S_{NH1}$  was 20 s, while that for  $S_{NH2}$  was 40 s.

### 2.2 Characterization of prepared surfaces

The surface morphologies were confirmed using a scanning electron microscope (SEM, Quanta 250, FEI) and the wettability of the prepared samples was determined by measuring the water contact angles (CA) and sliding angles (SA) using a contact angle meter (Model DM-50, Kyowa Interface Science Co., Ltd). The volume of a water droplet is 10.3  $\mu$ l.

### 2.3 Optical properties

The transparency and anti-reflective properties of the prepared surfaces were characterized using a UV-visible spectrometer (Cary 5000, Agilent Technologies) according to the incident angle. All prepared samples were compared with a bare quartz



**Table 1** Water hammer pressure ( $P_{WH}$ ) and dynamic pressure ( $P_D$ ) of the impacting droplets and spreading motion on  $S_{120}$ ,  $S_{350}$ ,  $S_{NH1}$ , and  $S_{NH2}$  according to Weber number

Weber number	Height (mm)	Impact velocity ( $\text{m s}^{-1}$ )	$P_{WH}$ (MPa)	$P_D$ (kPa)	Spreading motion
6	10	0.42	0.12	0.09	Flat disk
13	20	0.62	0.18	0.19	Flat disk
48	80	1.17	0.35	0.68	Flat disk
140	230	2.01	0.59	2.00	Wavy shape
290	450	2.97	0.86	4.14	Splash motion
416	670	3.63	1.03	5.94	Splash motion
673	980	4.38	1.30	9.61	Splash motion
854	1330	5.11	1.47	12.20	Splash motion

glass surface as a reference in the wavelength range of 350–1100 nm.

#### 2.4 Droplet impact experiment

Droplets (8.6  $\mu\text{l}$ ) were detached off under its weight at the tip of the needle from a syringe pump providing water, and fell onto the surfaces. Droplet impacts were recorded using a high-speed camera (Photron Ltd) at 3000 fps and shutter speed of 1/6400 s with a resolution of 512  $\times$  420 pixels. A high-speed camera was placed on the side of the glass. The droplet impact velocity was varied by changing the height of the 22-gauge nozzle. Based on the needle height, we evaluated the impact velocities as given in Table 1.

### 3. Results and discussion

The fabrication process for hierarchical nanostructures involves repeating basic colloidal lithography and reactive ion etching (RIE).<sup>38</sup> The process for fabricating hierarchical nanopillar

surfaces *via* multiple step colloidal lithography (MS-CL) is illustrated schematically in Fig. 1(a), and the resulting surfaces of each step are shown in the associated scanning electron microscopy (SEM) images in Fig. 1(b)–(e). Polystyrene nanoparticles (PS NPs) were employed as a mask to achieve the target morphology with the desired superhydrophobicity and low reflectivity for self-cleaning and transparency. The success of the surface patterning was determined by controlling the self-assembly of PS NPs and manipulating their monolayer packing. The floating method was used to pack particles on the surface,<sup>39</sup> enabling hexagonal packing of PS NPs at the air/water interface driven by surface tension and gravity, as shown in Fig. 1(b) and (d). We used commercial colloidal PS NPs having the sizes of  $120 \pm 7$  and  $350 \pm 14$  nm. This determined the 1st and 2nd base diameters of the nanopillars on the surface. Thereafter, anisotropic quartz glass etching was successively conducted in a mixture of  $\text{CF}_4$ ,  $\text{H}_2$ , and  $\text{O}_2$  gases, as shown in Fig. 1(c). The condition are described in detail in ref. 40. Finally, the remaining polystyrene nanoparticles on the structures were

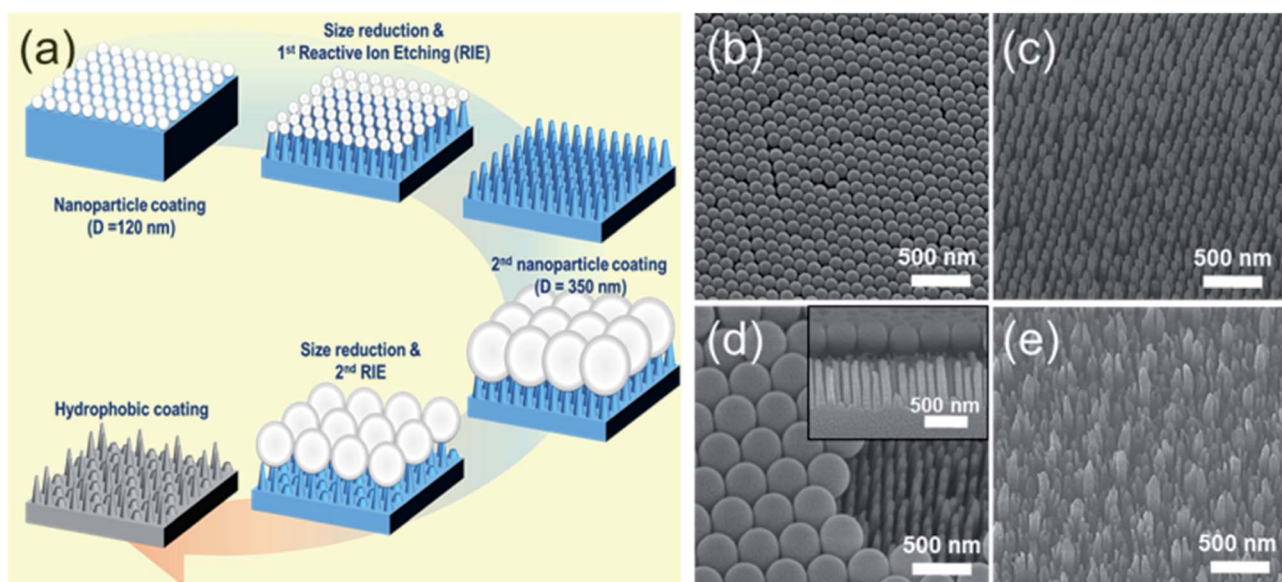


**Fig. 1** (a) Fabrication sequence for the hierarchical nanopillar array on quartz glass using two-step colloidal lithography with reactive ion etching method. 120 and 350 nm diameter polystyrene nanoparticles were used as a mask. The SEM images of (b) self-assembled monolayer of 120 nm PS NPs, (c) the surface after 1st RIE process using 120 nm PS NPs, (d) self-assembled monolayer of 350 nm PS NPs on top of the nanopillar surface shown in (c), and (e) the surface after 2nd RIE process using 350 nm PS NPs. The scale bar is 500 nm.



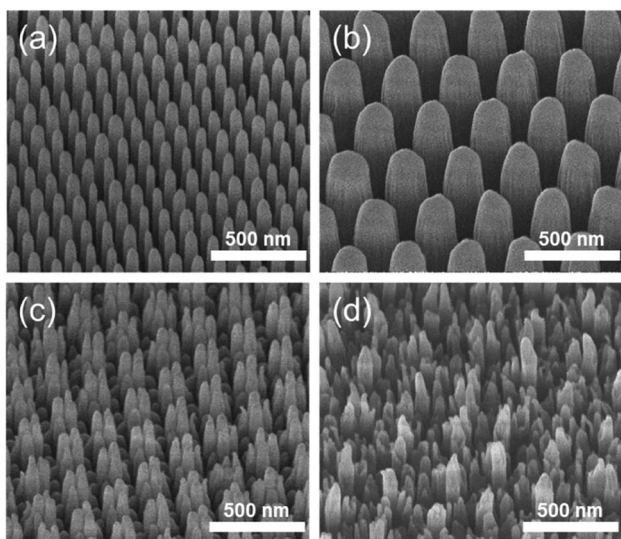


Fig. 2 Slightly tilted top SEM images of nanopillar array on quartz glass fabricated with colloidal lithography using (a) 120 nm PS NPs ( $S_{120}$ ), (b) 350 nm PS NPs ( $S_{350}$ ), (c) 120 and 350 nm PS NPs ( $S_{NH1}$ ) with 20 s size reduction time in the 2nd RIE process and (d) 120 and 350 nm PS NPs ( $S_{NH2}$ ) with 40 s size reduction time in the 2nd RIE process. The detailed fabrication conditions and morphology dimensions of nanopillar structures are described in the text.

removed using  $O_2$  plasma. Furthermore, to fabricate nanoscale hierarchical structures, the colloidal lithography of larger NPs than the 1st NPs was repeated using the same process. During etching, the prepared 1st nanopillars located below the 2nd NPs were protected from reactive ion etching, resulting in the fabrication of a hierarchically structured surface, as shown in Fig. 1(e). In summary, quartz glass was etched with a mask of monolayered 120 nm PS NPs at first and thereafter with 350 nm PS NPs. MS-CL can be repeated continuously with increasing NPs for multistage hierarchical structures. In addition, we could control the number of short nanopillars in the nanoscale hybrid structure by adjusting the size reduction time during the 2nd RIE process.

To obtain the dual functions of robust superhydrophobicity and omnidirectional broadband antireflective properties with hierarchical nanostructures, two types of samples were prepared with a combination of 120 and 350 nm NPs. Fig. 2 shows the SEM images of the mono-structured nanopillars,  $S_{120}$  and  $S_{350}$ , and hierarchical nanopillars,  $S_{NH1}$  and  $S_{NH2}$ . The morphology of the nanopillars was determined according to the size reduction and etching times. As the size reduction time of the PS NP is increased, sharp tip-shaped nanopillars are

obtained. The height of the nanopillars was linearly related to the etching time. Among the several etching processes used,  $S_{120}$  resulted in truncated cone-shaped nanopillars with a height of  $517 \pm 21$  nm, top diameter of  $82 \pm 6$  nm top, and bottom diameter of  $120 \pm 7$  nm, as shown in Fig. 2(a);  $S_{350}$  also led to truncated cone-shaped nanopillars with a height of  $678 \pm 28$  nm, top diameter of  $203 \pm 13$  nm, and bottom diameter of  $350 \pm 14$  nm, as shown in Fig. 2(b). The maximum gap between the top of the nanopillars was  $40 \pm 5$  nm for  $S_{120}$  and  $151 \pm 7$  nm for  $S_{350}$ . By contrast, the hierarchically structured samples had two different shapes of nanopillars by modulating the size reduction time of the 2nd NPs as 30 and 45 s for  $S_{NH1}$  and  $S_{NH2}$ , respectively. The reason for the difference between the short and long pillars is that the long pillars were not etched by the 350 nm PS NP mask in the 2nd RIE process. As a result, hierarchically structured samples such as  $S_{NH1}$  and  $S_{NH2}$  showed dissimilar morphologies based on the change in size of the 350 nm PS NP mask owing to the varied size reduction times in the 2nd RIE process. Therefore, while  $S_{NH1}$  has three to five grouped pillar structures,  $S_{NH2}$  has two to three grouped pillar structures. Furthermore,  $S_{NH1}$  led to long pillars with a height of  $682 \pm 12$  nm, top diameter of  $79 \pm 2$  nm, and maximum gap of  $154 \pm 3$  nm, and short pillars with a height of  $272 \pm 18$  nm height, top diameter of  $93 \pm 5$  nm, and maximum gap of  $40 \pm 3$  nm, as shown in Fig. 2(c). However,  $S_{NH2}$  shows the long pillars with a height of  $682 \pm 21$  nm, top diameter of  $78 \pm 2$  nm, and maximum gap of  $520 \pm 12$  nm, as well as the short pillars with a height of  $269 \pm 14$  nm, top diameter of  $103 \pm 9$  nm, and maximum gap of  $40 \pm 6$  nm, as shown in Fig. 2(d). Then, based on the maximum gaps of the samples, the contact area fraction ( $\Phi_C$ ) of the nanostructured samples was determined.  $\Phi_C$  of  $S_{120}$  and  $S_{350}$  were 0.42 and 0.29, respectively. By contrast, the hierarchically structured samples have two  $\Phi_C$  depending on the pillar height because the long pillars have a larger maximum gap than the short pillars. While the contact area fraction of  $S_{NH1}$  was 0.09 for long pillars and 0.54 for short pillars, the contact area fraction of  $S_{NH2}$  was 0.08 and 0.66 for long and short pillars, respectively, as listed in Table 2.

The water contact angle (CA) was measured to investigate the superhydrophobicity of the hierarchy. Because the physical structure and chemical coating determine the surface wettability, the samples were coated with perfluoropolyether (PFPE) *via* a simple dipping method. In the contact angle measurements, the water droplet did not adhere on the surface as shown in ESI Movie S1.† After observing that the water droplet hardly attached to the surface, the water contact angle values were measured in Table 2. The static, advancing, and receding contact angles of all samples were  $>160^\circ$ , suggesting that all

Table 2 Water contact angles and contact area fraction of  $S_{120}$ ,  $S_{350}$ ,  $S_{NH1}$ , and  $S_{NH2}$ . L and S indicate long pillars and short pillars, respectively

Sample	Contact angle (CA) (°)	Advancing CA (°)	Receding CA (°)	CA hysteresis (°)	Contact area fraction ( $\Phi_C$ )
$S_{120}$	$170.6 \pm 1.4$	$177.4 \pm 2$	$163.5 \pm 1.9$	$13.9 \pm 2.1$	0.42
$S_{350}$	$172.4 \pm 2$	$173.2 \pm 1.1$	$160.6 \pm 4$	$12.7 \pm 1.3$	0.29
$S_{NH1}$	$177.4 \pm 2.0$	$177.8 \pm 1$	$177.1 \pm 0.1$	$0.7 \pm 0.8$	0.09 (L), 0.54 (S)
$S_{NH2}$	$177.8 \pm 0.9$	$177.9 \pm 0.1$	$177.2 \pm 1.0$	$0.7 \pm 0.1$	0.08 (L), 0.66 (S)



cavities were filled with air. Furthermore, the surfaces with large cavity area fractions have a higher contact angle and lower hysteresis angle than the surfaces with small cavity area fractions. The contact angle hysteresis of  $S_{\text{NH}1}$  and  $S_{\text{NH}2}$  was  $0.7^\circ$ , which is  $10^\circ$  lower than the contact angle hysteresis of  $S_{120}$  and  $S_{350}$ . Based on these measured CAs, nanoscale hierarchically structured samples showed excellent water repellency, and a droplet could slide easily even with a small slope ( $\sim 1^\circ$ ) on  $S_{\text{NH}1}$  and  $S_{\text{NH}2}$ .

The optical properties of the nanopillar-structured surfaces were investigated considering their wide angular transmittance. The antireflection of nanostructures for photovoltaics or optical devices provides improved transmission and visual clarity in particular for a wide angle of incidence (AOI). According to Boden *et al.*, the reflection minima of the reflectance spectrum of a nanopillar array are related to the diameter of the nanopillar depending on the wavelength.<sup>35</sup> Moreover, because the height of the nanopillar affects the interference between the reflected light from its top and bottom, the wavelengths that cause the lowest reflection can be adjusted depending on the height.<sup>40</sup> Therefore, the formation of nanoscale hierarchical structures with different diameters or heights can be an effective strategy to improve the antireflection effect.<sup>41,42</sup> Furthermore, the benefits achieved by the periodic arrangement of nanostructures, such as low scattering loss in the short wavelength range, can be maintained.<sup>43</sup> Considering these aspects, the fabricated nano-hierarchical structure offers great advantages in achieving high antireflectivity performance owing to its controllability.

Fig. 3(a) shows photographs of the quartz glass under light exposure. All samples exhibit an antireflective effect, so that the letters below the glasses are clearly observed. However, the visibility varies slightly with different characteristics according to the nanopillar morphologies. Therefore, the transmittance was measured using a spectrophotometer in the configuration shown in Fig. 3(b). Although the transmittance of  $S_{\text{NH}1}$  is almost identical to that of  $S_{350}$  in the short-wavelength range, a broadband enhancement compared to  $S_{350}$  is observed at normal incidence, as shown in Fig. 3(c).  $S_{\text{NH}2}$  that has an increased number of short pillars on the top, exhibited a significant enhancement in the transmittance for the short-wavelength range compared to  $S_{\text{NH}1}$  and  $S_{350}$ . This implies that reducing the number of short nanopillars is effective in diminishing size-dependent incoherent backward scattering. In addition,  $S_{\text{NH}2}$  also exhibited slightly better properties than  $S_{120}$  at long wavelengths owing to the existence of a 350 nm size morphology. When the AOI was  $70^\circ$ ,  $S_{\text{NH}2}$  still demonstrated the best antireflective effect, as shown in Fig. 3(d). Moreover, the improvement in transmittance due to the nanoscale hierarchical structure becomes more pronounced as the AOI increases. For example,  $S_{\text{NH}1}$  has an identical transmittance in the short-wavelength range to that of  $S_{350}$  for normal incidence, while the transmittance of  $S_{\text{NH}1}$  for an AOI of  $70^\circ$  is higher than that of  $S_{350}$ . This better angular antireflective effect of the nano-hierarchical structure can be explained by the decrease in the scattering area. In the case of normal incidence, the difference in the area that produced light scattering between  $S_{\text{NH}1}$  and  $S_{350}$

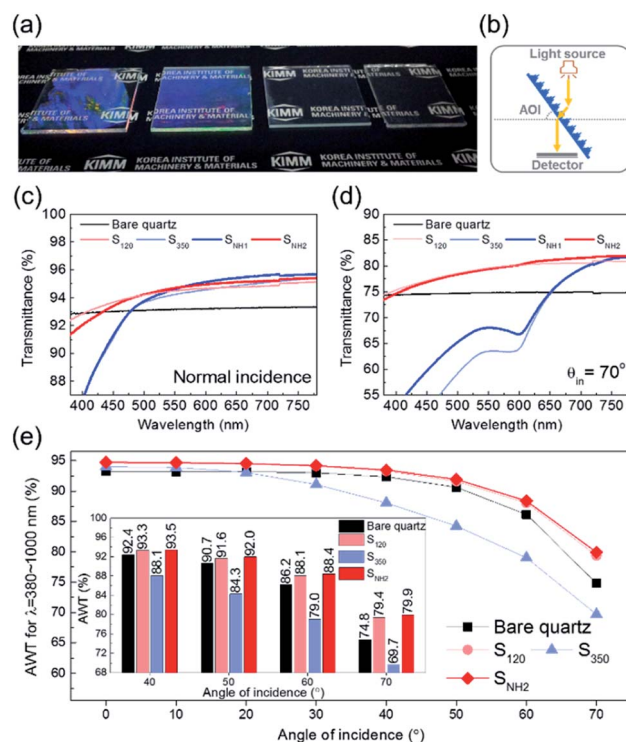


Fig. 3 Angle of incidence (AOI) dependent optical properties of nanopillar structured glasses. (a) Photographic images of nanostructured glasses, (b) measurement setup of AOI dependent transmittance, (c and d) specular transmittance of nano-textured glasses at AOI =  $5^\circ$  and  $70^\circ$  respectively, (e) average weighted transmittance (AWT) values of samples as a function of AOIs for 380–1000 nm wavelengths (the inset represents the AWT values of each sample for 40–70° of AOIs in order to show high angle AR effect of nano-hierarchical structure numerically). Because the aim of this work is to demonstrate the enhanced high angle antireflective effect via effective nanoscale hierarchical structuring, the results for  $S_{\text{NH}2}$  are only compared with the other mono-structures and the bare quartz substrate.

was negligible, allowing a similar transmittance to be observed over the short-wavelength range. However, for an AOI of  $70^\circ$ ,  $S_{\text{NH}1}$  provides a more reduced scattering area than  $S_{350}$ ; thus, its transmittance increased. In Fig. 3(e), the values of the average weighted transmittance (AWT) of the samples used in this work are presented as a function of AOIs to show a broadband improvement of the high-angle antireflective effect owing to nanoscale hierarchical structuring. The values of AWT were obtained using  $\int T(\lambda)I(\lambda)_{\text{AM1.5G}}d\lambda / \int I(\lambda)_{\text{AM1.5G}}d\lambda$ , where  $T(\lambda)$  is the measured transmittance and  $I(\lambda)_{\text{AM1.5G}}$  is the standard terrestrial solar irradiance.<sup>44</sup> Because  $S_{\text{NH}2}$  has a better angular antireflective effect than  $S_{\text{NH}1}$  owing to its effective design that avoids undesirable scattering, only  $S_{\text{NH}2}$  was compared with the bare quartz and the other mono-structures as shown in Fig. 3(e).  $S_{350}$  exhibited a lower performance in angular antireflective effects than the other samples due to significant scattering loss in the short-wavelength region. However,  $S_{350}$  exhibits good antireflective properties in the infrared range because the size of the nanostructure corresponds to the subwavelength scale. Although  $S_{\text{NH}2}$  appears to have little difference in AWT values



compared to  $S_{120}$ ,  $S_{NH2}$  consistently showed improved AWT values over  $S_{120}$  for 50–70° AOIs, as shown in the inset of Fig. 3(e). In particular, when the AOI was 70°,  $S_{NH2}$  showed a 0.6% improvement in AWT compared to  $S_{120}$ . This means that  $S_{NH2}$  clearly shows a larger scattering than  $S_{120}$  for the short-wavelength region, but compensates for the scattering loss by broadband transmittance improvements using dual periodicity. Consequently,  $S_{NH2}$  exhibits a superior high-angle antireflective performance than  $S_{120}$  for broadband wavelengths. Therefore, considering the results of the above investigations on the angular antireflective effect, it is concluded that the reduced scattering area and the dual periodicity are the primary merits of the nano-hierarchical structure to achieve a better antireflective effect for the broadband wavelengths and wide AOIs.

The non-wetting property of the samples was evaluated in depth by analyzing water bouncing behavior to understand the aspect of the hierarchy. The superhydrophobic wetting state is categorized by the Wenzel state or the Cassie–Baxter state. In the Wenzel state, a water droplet follows surface asperity,<sup>45</sup> wherein the water droplet is strongly pinned onto the contact area, specifically at the edges of the structures. By contrast, in the Cassie–Baxter state, because a water droplet sits on the top of the surface structures, the surface area in contact with the solid surface is small.<sup>45</sup> This generates the liquid–gas interface where the adhesive force is absent, forming on a gas layer below the droplet. In addition, a water droplet in the Cassie–Baxter state can be easily removed from the surface because it has a smaller adhesive area than that in the Wenzel state. The droplet impact experiment allows for different spreading and bouncing motions according to the extent of non-wetting and mostly induces the wetting transition from the Cassie–Baxter to the Wenzel state. Therefore, the investigation of impact behavior is useful for determining the non-wetting ability, particularly for superhydrophobic surfaces with high contact angles. When an impacted droplet is in the Wenzel state, the droplet is pinned on the surface or bounces off, leaving small droplets on the surface. Alternatively, when an impacted droplet is in the Cassie–Baxter state, the structural gap creates capillary pressure that pushes water out with fast contact time and without a splash. Table 1 summarizes the spreading motion with various impact velocities and Weber numbers ( $We = \rho v^2 D / \sigma$ ) of the impacting droplets for different impact heights, calculated hammer pressures ( $P_{WH}$ ), and dynamic pressures ( $P_D$ ).<sup>46</sup> In the definition of Weber numbers,  $\rho$  is the droplet density,  $v$  is the droplet impact velocity,  $D$  is the droplet diameter, and  $\sigma$  is the liquid surface tension. When the droplet is impacted, pressures are balanced on the hierarchical nanosurface,  $P_{WH}$ ,  $P_D$ , and capillary pressure ( $P_C$ ), as described in Fig. 4(a).  $P_{WH}$  is generated by compression waves during the droplet impact, and  $P_D$  is caused by kinetic energy. To prevent the penetration of water into the gap,  $P_C$  is created by the surface tension between the structures on the surface during impact. The two pressures applied at the direction normal to the surface by impact are  $P_{WH}$  and  $P_D$  and are expressed as

$$P_{WH} \approx 0.2\rho cv, \quad (1)$$

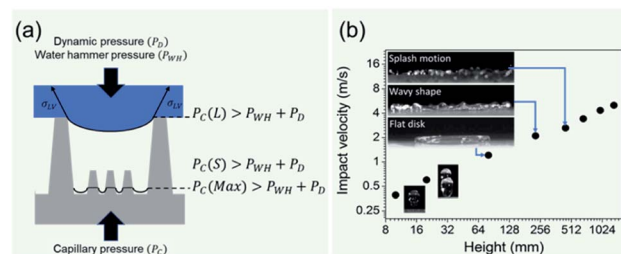


Fig. 4 (a) Schematics of pressure balance of dynamic pressure, water hammer pressure, and capillary pressure. (b) Water bouncing behavior according to impact velocity.

$$P_D = 0.5\rho v^2, \quad (2)$$

where  $\rho$  is the density of water,  $c$  is the speed of sound in water ( $\sim 1490 \text{ m s}^{-1}$ ), and  $v$  is the impact velocity.  $P_C$  is created by the surface tension between the structures of the surface during impact as<sup>47</sup>

$$P_C = -2\sigma \cos \theta / g_s, \quad (3)$$

where  $\sigma$  is the surface tension of the liquid,  $\theta$  is the contact angle, and  $g_s$  is the gap between the nanostructures. In this study, owing to the colloidal lithography of the hexagonally packed PS beads as a mask,  $g_s$  can be expressed using the structure diameter ( $D$ ) and the contact area fraction ( $\Phi_C$ ) as

$$\Phi_C = \frac{0.5\pi D^2}{\sqrt{3}(D + g_s)^2}, \quad (4)$$

Then,  $g_s$  and  $P_C$  are

$$g_s = \sqrt{\frac{\pi D^2}{2\sqrt{3}\Phi_C}} - D, \quad (5)$$

$$P_C = -2\sigma \cos \theta / \left( \sqrt{\frac{\pi D^2}{2\sqrt{3}\Phi_C}} - D \right). \quad (6)$$

Varanasi *et al.* showed the wetting state by balancing the water hammer pressure, dynamic pressure, and capillary pressure.<sup>48</sup> When the pressure condition was  $P_{WH} > P_D > P_C$ , the impacted droplet was in a Wenzel state, whereas when the pressure condition was  $P_{WH} > P_C > P_D$ , the impacted droplet was in a partial pinning state. Furthermore, when the pressure condition was  $P_C > P_{WH} > P_D$ , the impacted droplet was in a Cassie–Baxter state. Because all surfaces have truncated conical nanostructures as a result of colloidal lithography, the capillary pressure varies depending on the height of the structure. Unlike  $S_{120}$  and  $S_{350}$ ,  $S_{NH1}$  and  $S_{NH2}$  have two different capillary pressures and maximum capillary pressures because they have truncated conical structures of different heights. The values of maximum capillary pressures were 8.08 MPa for  $S_{350}$  and 23.97 MPa for  $S_{120}$ ,  $S_{NH1}$ , and  $S_{NH2}$ , respectively. Based on the calculated pressure values of  $P_{WH}$  (0.12–1.47 MPa),  $P_D$  (0.12–1.47 kPa), and the maximum  $P_C$  (8.08–23.97 MPa), it is inferred



that the impacted water droplets were in the Cassie–Baxter state. As shown in Fig. 4(b) and Table 1, the first spreading motion of impacted droplets were of three typical types; flat disk, wavy shape, and splash motion depending on the impact velocity (*i.e.* Weber number), regardless of the sample. The movie of droplet impact motion on  $S_{\text{NH}2}$  at different dropped heights of 80, 230, and 450 mm (*i.e.* Weber number; 48, 140, and 290) is available in ESI Movie S2.† For a Weber number  $<48$ , the spreading shape was flat disk. When the Weber number was

140, the spreading shape changed from a flat disk to a wavy shape and for a Weber number  $\geq 290$ , the spreading motions on all surfaces were wavy, and the impacted droplets then splashed. The critical velocity of the droplet breakup was  $2.97 \text{ m s}^{-1}$ .

This behavior proves that all of the nanostructured samples showed excellent superhydrophobicity. The detailed image sequences of Weber numbers 48, 140, 290, and 416 at 4 ms intervals up to 16 ms are displayed for the analysis of the impact

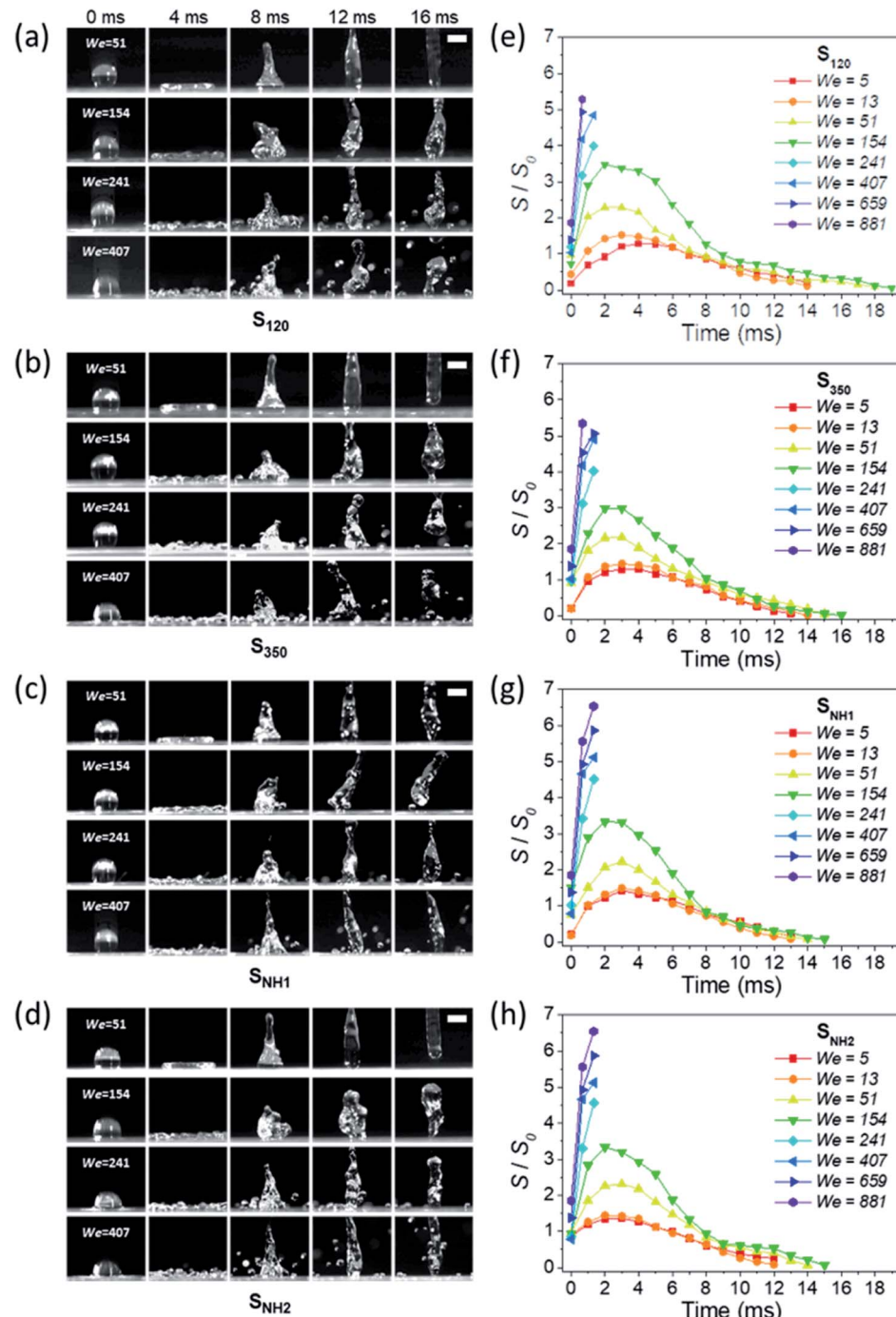


Fig. 5 Time sequence images of water droplet impact on the surface of (a)  $S_{120}$ , (b)  $S_{350}$ , (c)  $S_{\text{NH}1}$ , and (d)  $S_{\text{NH}2}$ . The scale bar is 2 mm. The ratio of the spreading diameter ( $S$ ) to initial droplet diameter ( $S_0$ , 2.542 mm) over time on (e)  $S_{120}$ , (f)  $S_{350}$ , (g)  $S_{\text{NH}1}$ , and (h)  $S_{\text{NH}2}$ .



behavior in Fig. 5(a)–(d). Water droplets show the representative motion of impact, spreading, recoiling, and rebound. The spreading motion and diameter of the samples show different behaviors according to the Weber number and surface wetting property in 4 ms images, and all droplets recoiled and rebounded at 8 ms. Furthermore, from the images, it is observed that the extent of rebounding was slightly different, in particular, for the splash behavior at high Weber numbers of 290 and 416. Depending on the Weber number, not only the spreading motion but also the spreading diameter changed. Fig. 5(e)–(h) show the spreading diameters and contact time of the impacted droplets depending on the Weber number. As the Weber number increased, the maximum spreading diameter increased, and the contact time, which is the time required for the bouncing process, increased owing to the increase in contact area where the friction force acts. Among the surfaces,  $S_{NH2}$  had shorter contact times than the others. In addition, for Weber number above 290, the impacted droplets splashed and separated into small droplets and then rebounded from the surfaces with changed mass. On the  $S_{NH1}$  and  $S_{NH2}$  surfaces, larger spreading diameters of the impacted droplets were observed than those on  $S_{120}$  and  $S_{350}$ .

The excellent performance of the hierarchical nanostructures of  $S_{NH1}$  and  $S_{NH2}$  was investigated in terms of the maximum spreading diameter, number of bounces, and effective slip length, as shown in Fig. 6. Fig. 6(a) and (b) show the comparison of the maximum spreading diameter and the number of bounces of each sample according to the Weber number, respectively. The maximum spreading diameter decreased in the order of  $S_{NH2}$ ,  $S_{NH1}$ ,  $S_{350}$ , and  $S_{120}$ . When the weber number was 881, the value of maximum spreading diameter ( $S_M$ ) is 42.30, 42.22, 34.54, and 34.15 mm for  $S_{NH2}$ ,  $S_{NH1}$ ,  $S_{350}$ , and  $S_{120}$ , respectively. The maximum spreading diameter of  $S_{NH1}$  and  $S_{NH2}$  is 1.2 times larger than that of  $S_{120}$  and  $S_{350}$ . Furthermore, the impacted droplets on  $S_{NH2}$  had the

highest number of bounces; in particular, when the Weber number was 6, the water droplets bounced 14 times on  $S_{NH2}$ , 12 times on  $S_{NH1}$ , 6 times on  $S_{350}$ , and 6 times on  $S_{120}$  as shown in ESI Movie S3.† Furthermore, as the Weber number increased, the number of bounces decreased owing to severe splash behavior. These behaviors clearly indicate that nanoscale hierarchical structures contribute to non-wetting properties, even with dynamic water droplets. The superior bouncing property of nano-hierarchical surfaces can be explained by the slip length as an indicator to elucidate the bouncing behavior on superhydrophobic surfaces. The spreading diameter of the samples is affected by friction during spreading and recoiling as the energy loss of the impacted droplet is minimized with a low friction interaction. Friction force is the force generated by the no-slip boundary condition in the liquid–solid interaction.<sup>49</sup> On a smooth surface, the friction force is defined as

$$F_f = A\eta\gamma_s, \quad (7)$$

where  $A$  is the area of the spreading water,  $\eta$  is the shear viscosity of water, and  $\gamma_s$  is the shear rate on the solid patch. Owing to the shear rate, the velocity of the fluid, called the slip velocity,  $V$ , varies along the  $z$ -axis. Fig. 6(c) illustrates that the slip velocity varies depending on the boundary conditions such as no slip, partial slip, and preface slip. The boundary condition is expressed as slip length  $b$ . Considering the slip velocity and slip length, the friction force is given by

$$F_f = A\eta\frac{V}{b}, \quad (8)$$

The spreading and recoil process on the superhydrophobic surface with the Cassie–Baxter state has two boundary conditions owing to the contact and gas areas. During the spreading and recoiling of water, the area of the pillars induces a no-slip boundary condition, whereas the gas area induces a perfect slip boundary condition on the liquid–vapor interface. The friction force on a superhydrophobic surface is defined as

$$F_f = A\Phi C\eta\dot{\gamma}_s, \quad (9)$$

where  $\dot{\gamma}_s$  is the average shear rate of the solid patch. To estimate  $\dot{\gamma}_s$ , the velocity profile in the liquid is influenced by the solid zones only in a region of size  $0.5D$ .

$$\dot{\gamma}_s \sim 2U/D, \quad (10)$$

where  $U$  is the velocity of the fluid in the free-slip zones. Therefore,  $F_f \equiv 2A(\Phi_C)\eta U/D$ . The heterogeneity of the boundary conditions is expressed by the effective slip length ( $b_{eff}$ ), which is defined by  $F_f = A\eta V/b_{eff}$ <sup>48</sup> as shown in Fig. 6(d).

$$b_{eff} = \alpha \frac{D}{2(\Phi_C)}, \quad (11)$$

using eqn (4),

$$b_{eff} = \alpha \frac{\sqrt{3}D}{\pi} \left(1 + \frac{g_s}{D}\right)^2, \quad (12)$$

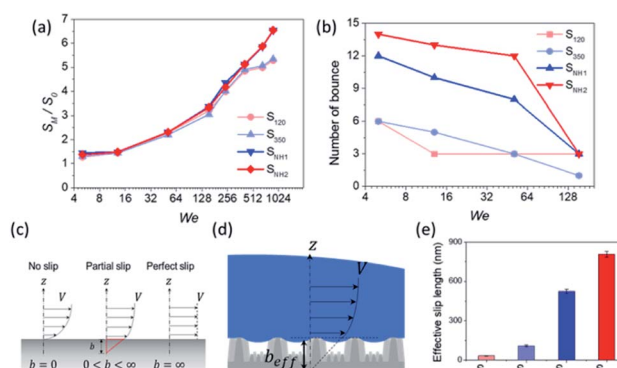


Fig. 6 a) Ratio of the maximum spreading diameter ( $S_M$ ) to initial droplet diameter ( $S_0$ , 2.542 mm) on all surfaces. (b) The number of bounces of 8.6  $\mu$ l droplet on the surfaces when Weber number is  $\leq 140$ . (c) The schematics of slip velocity and slip length according to boundary condition; no slip, partial slip, and perfect slip. (d) The schematics of effective slip length due to the heterogeneity of boundary conditions on structures. (e) The calculated effective slip length of the surfaces.



Table 3 Water contact angle, critical velocity, number of bouncing, and calculated slip length of various surfaces as reported

Structure	CA (°)	Critical velocity (m s <sup>-1</sup> )	Number of bouncing	Slip length (nm)
Nano-hierarchical structure <sup>This study</sup>	178	2.97	14	800
Flat <sup>51</sup>	120			25–100
Rough surface <sup>52</sup>	120			50–350
Porous structure <sup>53</sup>	130	1.14		
Rough surface <sup>54</sup>	120–150		2–16	
Hierarchical structure <sup>55</sup>	154	1.41		
Micro structure <sup>56</sup>	156	2		
Micro structure <sup>57</sup>	157	1.34		
Rough surface <sup>58</sup>	160	2.1		
Hierarchical structure <sup>59</sup>	164	1.97		
Hierarchical structure <sup>60</sup>	164	2.95		
Nano structure <sup>61</sup>	165			0–1500
Hierarchical structure <sup>62</sup>	166	2.24		
Porous structure <sup>63</sup>	169		7	
Porous structure <sup>64</sup>	175		14	

The previous result shows that, in the case of patterned no-slip dots,  $1/\pi$  is appropriate as a prefactor,  $\alpha$ , of the predicted relationship.<sup>50</sup>

$$b_{\text{eff}} \approx \frac{\sqrt{3}D}{\pi^2} \left(1 + \frac{g_s}{D}\right)^2, \quad (13)$$

The results calculated using the equation are shown in Fig. 6(e) and ESI Table S1† with values of minimum and maximum capillary pressure ( $P_C$ ). The effective slip length of  $S_{\text{NH}2}$  was found to be the longest. Therefore, the friction force on  $S_{\text{NH}2}$  is smaller than that of the others and provides the highest number of bounces among the reported numbers. Consequentially, based on the several analyses of bouncing behavior, it is suggested that the contact time, spreading diameter, and spreading shape of the bouncing behavior do not precisely correlate with the excellence of the hierarchical structures, while the effective slip length distinguishes between the superhydrophobic samples. To date, the reports on the water impact behavior, critical velocity, number of bounces, and slip length, for understanding superhydrophobicity have been scarce. Table 3 summarizes the various superhydrophobic surfaces with different wetting characteristics. Based on the analysis of these results, nanohierarchy provides excellent superhydrophobicity, resulting in a high critical velocity and a large number of bounces with two-tier morphology for large capillary pressure and long effective slip length. Because the mechanical robustness of the nanopillar structured surfaces was confirmed against finger rubbing,<sup>65,66</sup> these functional surfaces is promising in the practical applications.

## 4. Conclusions

Inspired by the lotus leaf and moth-eye, nanoscale hierarchical pillars were fabricated *via* multiple step colloidal lithography with 120 and 350 nm polystyrene nanoparticles. First, the smaller nanopillars were fabricated, and then the larger nanoparticles were used as a mask in the subsequent etching

process. Upon repeating these steps, hierarchical structures can be obtained regardless of size. Four fabricated nanosurfaces, mono-pillared  $S_{120}$  and  $S_{350}$ , and hierarchical-pillared  $S_{\text{NH}1}$  and  $S_{\text{NH}2}$ , exhibited superhydrophobicity. Notably,  $S_{\text{NH}2}$  and  $S_{\text{NH}1}$  have water contact angles of 177° and a sliding angle of 1°.  $S_{\text{NH}2}$  with a 120 nm morphology hierarchical surface exhibited the best antireflective effect among the samples by decreasing the scattering area, in particular, when the angle of incidence increased. Therefore,  $S_{\text{NH}2}$  has a transmittance of 80% at an incidence angle of 70°. The water bouncing behavior of the samples demonstrated the superiority of the non-wetting behavior of the surfaces, showing the advantages of hierarchy. The values of the maximum capillary pressures were calculated as 23.97 MPa for 120 nm morphology-based samples;  $S_{120}$ ,  $S_{\text{NH}1}$ , and  $S_{\text{NH}2}$ . Furthermore, the impacted droplets for the Weber number above 290 were splashed and the critical velocity of droplet breakup was obtained as 2.97 m s<sup>-1</sup> for all samples. Furthermore, the impacted droplets on  $S_{\text{NH}2}$  had the highest number of bounces, 14 times at Weber number 6, and largest maximum spreading diameter of 42.30 mm among the samples. These observations can be explained by the effective slip length. In particular, these results provide a valuable contribution by maintaining the transparency overcoming the hierarchy in microstructures. Therefore, the presented nanoscale hierarchical surface displays outstanding potential for superhydrophobicity and wide angular transmittance, demonstrating extreme water bouncing behavior. Hierarchy in nature results in unique multifunctionality, and multiple step colloidal lithography can potentially be used to formulate such structures, specifically at the nanoscale.

## Author contributions

Both authors (C. L. and S. J.) contributed equally as first authors to fabricate the sample and measure the properties. S. J. conceived and designed the experiments. C. L. performed the analysis. S. O. and S. P. provided critical suggestions. Y. J improved the manuscript. J. L. reviewed and improved the



manuscript. H. L. conceived and supervised the project. All authors reviewed and commented on the manuscript.

## Conflicts of interest

There are no conflicts to declare.

## Acknowledgements

This research was supported by the Korea Institute of Energy Technology Evaluation and Planning. Financial resources were granted by the Ministry of Trade, Industry & Energy, Republic of Korea (20193010014740), the Korea Environment Industry & Technology Institute through its Ecological Imitation-based Environmental Pollution Management Technology Development Project and funded by the Korea Ministry of Environment (2019002790005), and National Research Foundation grant by the Ministry of Education, under “Basic Science Research Program” (NRF-2017R1D1A1B04033182).

## Notes and references

- V. A. Ganesh, H. K. Raut, A. S. Nair and S. Ramakrishna, *J. Mater. Chem.*, 2011, **21**, 16304.
- S. Nishimoto and B. Bhushan, *RSC Adv.*, 2013, **3**, 671.
- X. Li, G. Wang, A. S. Moita, C. Zhang, S. Wang and Y. Liu, *Appl. Surf. Sci.*, 2020, **505**, 144386.
- L. J. Chen, M. Chen, H. Di Zhou and J. M. Chen, *Appl. Surf. Sci.*, 2008, **255**, 3459.
- B. L. Feng, S. Li and Y. Li, *Adv. Mater.*, 2016, **14**, 1857.
- M. Sun, C. Luo, L. Xu, H. Ji, Q. Ouyang, D. Yu and Y. Chen, *Langmuir*, 2005, **21**, 8978.
- I. You, T. G. Lee, Y. S. Nam and H. Lee, *ACS Nano*, 2014, **8**, 901.
- J. Yong, F. Chen, Q. Yang, Y. Fang, J. Huo, J. Zhang and X. Hou, *Adv. Mater. Interfaces.*, 2017, **4**, 1700552.
- X. Dai, N. Sun, S. O. Nielsen, B. B. Stogin, J. Wang, S. Yang and T. S. Wong, *Sci. Adv.*, 2018, **4**, 1.
- J. Zhang, A. Wang and S. Seeger, *Adv. Funct. Mater.*, 2014, **24**, 1074.
- T. S. Wong, S. H. Kang, S. K. Y. Tang, E. J. Smythe, B. D. Hatton, A. Grinthal and J. Aizenberg, *Nature*, 2011, **477**, 443.
- K. Hadobas, S. Kirsch, A. Carl, M. Acet and E. F. Wassermann, *Nanotechnology*, 2000, **11**, 161.
- W. K. Kuo, G. F. Kuo, S. Y. Lin and H. Yu, *Bioinspiration Biomimetics*, 2015, **10**, 56010.
- W. K. Kuo, J. J. Hsu, C. K. Nien and H. H. Yu, *ACS Appl. Mater. Interfaces*, 2016, **8**, 32021.
- W. K. Kuo, S. Y. Lin, S. W. Hsu and H. H. Yu, *Opt. Mater.*, 2017, **66**, 630.
- D. Yoo, S. C. Park, S. Lee, J. Y. Sim, I. Song, D. Choi, H. Lim and D. S. Kim, *Nano Energy*, 2019, **57**, 424.
- J. Huang, X. Wang and Z. L. Wang, *Nano Lett.*, 2006, **6**, 2325–2331.
- W. Lee, M. K. Jin, W. C. Yoo and J. K. Lee, *Langmuir*, 2004, **20**, 7665.
- X. Zeng, L. Qian, X. Yuan, C. Zhou, Z. Li, J. Cheng, S. Xu, S. Wang, P. Pi and X. Wen, *ACS Nano*, 2017, **11**, 760.
- X. Gou and Z. Guo, *Langmuir*, 2020, **36**, 64.
- L. T. Nguyen, Z. Bai, J. Zhu, C. Gao, X. Liu, B. T. Wagaye, J. Li, B. Zhang and J. Guo, *ACS Omega*, 2021, **6**, 3910.
- Y. Liu, H. Gu, Y. Jia, J. Liu, H. Zhang, R. Wang, B. Zhang, H. Zhang and Q. Zhang, *Chem. Eng. J.*, 2019, **356**, 318.
- X. Li, J. Deng, H. Yue, D. Ge and X. Zou, *Tribol. Int.*, 2019, **134**, 240.
- H. W. Chien, X. Y. Chen, W. P. Tsai and M. Lee, *Colloids Surf. B*, 2020, **186**, 110738.
- A. G. Domel, G. Domel, J. C. Weaver, M. Saadat, K. Bertoldi and G. V. Lauder, *Bioinspiration Biomimetics*, 2018, **13**, 056014.
- T. Zhu, Y. Cheng, J. Huang, J. Xiong, M. Ge, J. Mao, Z. Liu, X. Dong, Z. Chen and Y. Lai, *Chem. Eng. J.*, 2020, **399**, 125746.
- S. S. Latthe, R. S. Sutar, V. S. Kodag, A. K. Bhosale, A. M. Kumar, K. Kumar Sadasivuni, R. Xing and S. Liu, *Prog. Org. Coat.*, 2019, **128**, 52.
- S. P. Dalawai, M. A. Saad Aly, S. S. Latthe, R. Xing, R. S. Sutar, S. Nagappan, C. S. Ha, K. Kumar Sadasivuni and S. Liu, *Prog. Org. Coat.*, 2020, **138**, 105381.
- H. K. Raut, V. A. Ganesh, A. S. Nair and S. Ramakrishna, *Energy Environ. Sci.*, 2011, **4**, 3779.
- S. Chattopadhyay, Y. F. Huang, Y. J. Jen, A. Ganguly, K. H. Chen and L. C. Chen, *Mater. Sci. Eng., R*, 2010, **69**, 1.
- K. H. Kim and Q. H. Park, *Sci. Rep.*, 2013, **3**, 1062.
- K. C. Park, H. J. Choi, C. H. Chang, R. E. Cohen, G. H. McKinley and G. Barbastathis, *ACS Nano*, 2012, **6**, 3789.
- Y. Lin, J. Han, M. Cai, W. Liu, X. Luo, H. Zhang and M. Zhong, *J. Mater. Chem. A*, 2018, **6**, 9049.
- W. S. Chu, C. S. Kim, H. T. Lee, J. O. Choi, J. Il Park, J. H. Song, K. H. Jang and S. H. Ahn, *Int. J. Precis. Eng. Manuf. - Green Technol.*, 2014, **1**, 75.
- S. A. Boden and D. M. Bagnall, *Appl. Phys. Lett.*, 2008, **93**, 1.
- X. Xu, Q. Yang, N. Wattanatorn, C. Zhao, N. Chiang, S. J. Jonas and P. S. Weiss, *ACS Nano*, 2017, **11**, 10384.
- X. Fang, C. Zheng, Z. Yin, Z. Wang, J. Wang, J. Liu, D. Luo and Y. J. Liu, *ACS Appl. Mater. Interfaces*, 2020, **12**, 12345.
- H. Lim, S. Ji and W. D. Kim, (Korean Institute of Machinery & Materials) Patterning Method for Nano-Structure, KR patent 10-2009-0127387. 2009.
- S. C. Park, N. Kim, S. Ji and H. Lim, *Microelectron. Eng.*, 2016, **158**, 35.
- S. Ji, J. Park and H. Lim, *Nanoscale*, 2012, **4**, 4603.
- K. Watanabe, J. Yamamoto and R. Tsuchiya, *J. Appl. Phys.*, 2015, **118**, 085102.
- L. Yang, Q. Feng, B. Ng, X. Luo and M. Hong, *Appl. Phys. Express*, 2010, **3**, 5.
- S. Ji, K. Song, T. B. Nguyen, N. Kim and H. Lim, *ACS Appl. Mater. Interfaces*, 2013, **5**, 10731.
- National Renewable Energy Laboratory (NREL), *Reference Air Mass 1.5 Spectra*, accessed June 5, 2021, <https://www.nrel.gov/grid/solar-resource/spectra-am1.5.html>.
- D. Quéré and M. Reyssat, *Philos. Trans. R. Soc., A*, 2008, **366**, 1539.
- O. G. Engel, *J. Res. Natl. Bur. Stand.*, 1955, **54**, 281.



47 H. Kim and S. H. Kim, *Langmuir*, 2018, **34**, 5480.

48 K. K. Varanasi, T. Deng, M. Hsu and N. Bhate, *Tech. Proc. 2009 NSTI Nanotechnol. Conf. Expo, NSTI-Nanotech 2009*, vol. 3, p. 184.

49 L. Bocquet and J. L. Barrat, *Soft Matter*, 2007, **3**, 685.

50 C. Ybert, C. Barentin, C. Cottin-Bizonne, P. Joseph and L. Bocquet, *Phys. Fluids*, 2007, **19**, 123601.

51 P. Huang, J. S. Guasto and K. S. Breuer, *J. Fluid Mech.*, 2006, **566**, 447.

52 T. Schmatko, H. Hervet and L. Leger, *Phys. Rev. Lett.*, 2005, **94**, 244501.

53 C. Y. Chiang, T. Y. Yang, A. Casandra and S. Y. Lin, *Exp. Therm. Fluid Sci.*, 2017, **88**, 444.

54 F. J. M. Ruiz-Cabello, P. F. Ibáñez-Ibáñez, J. F. Gómez-Lopera, J. Martínez-Aroza, M. Cabrerizo-Vílchez and M. A. Rodríguez-Valverde, *J. Colloid Interface Sci.*, 2017, **508**, 129.

55 P. Hao, C. Lv, F. Niu and Y. Yu, *Sci. China: Phys., Mech. Astron.*, 2014, **57**, 1376.

56 R. Zhang, P. Hao, X. Zhang, F. Niu and F. He, *Langmuir*, 2018, **34**, 7942.

57 C. Guo, D. Zhao, Y. Sun, M. Wang and Y. Liu, *Langmuir*, 2018, **34**, 3533.

58 E. S. Quintero, G. Riboux and J. M. Gordillo, *J. Fluid Mech.*, 2019, **870**, 175.

59 L. Chen, Z. Xiao, P. C. H. Chan, Y. K. Lee and Z. Li, *Appl. Surf. Sci.*, 2011, **257**, 8857.

60 H. Kim and S. H. Kim, *Langmuir*, 2018, **34**, 5480.

61 P. Joseph, C. Cottin-Bizonne, J. M. Benoit, C. Ybert, C. Journet, P. Tabeling and L. Bocquet, *Phys. Rev. Lett.*, 2006, **97**, 156104.

62 M. Abolghasemibizaki and R. Mohammadi, *J. Colloid Interface Sci.*, 2018, **509**, 422.

63 Z. Xu, D. Jiang, F. Wu, X. Guo, Z. Wei and J. Chen, *J. Mater. Sci.*, 2018, **53**, 5364.

64 C. R. Crick and I. P. Parkin, *Chem. Commun.*, 2011, **47**, 12059.

65 J. Park, H. Lim, W.-D. Kim and J. S. Ko, *J. Colloid Interface Sci.*, 2011, **360**, 272.

66 I. D. Jung, M. C. Lee, H. Lim, E. Smela and J. S. Ko, *Appl. Surf. Sci.*, 2015, **349**, 705.

